



# Direct coordination of pterin to Fe<sup>II</sup> enables neurotransmitter biosynthesis in the pterin-dependent hydroxylases

Shyam R. Iyer<sup>a</sup>, Kasper D. Tidemand<sup>b</sup>, Jeffrey T. Babicz Jr<sup>a</sup>, Ariel B. Jacobs<sup>a</sup>, Leland B. Gee<sup>a</sup>, Lærke T. Haahr<sup>b</sup>, Yoshitaka Yoda<sup>c</sup>, Masayuki Kurokuzu<sup>d</sup>, Shinji Kitao<sup>d</sup>, Makina Saito<sup>d</sup>, Makoto Seto<sup>d</sup>, Hans E. M. Christensen<sup>b,e</sup>, Günther H. J. Peters<sup>b</sup>, and Edward I. Solomon<sup>a,1</sup>

<sup>a</sup>Department of Chemistry, Stanford University, Stanford, CA 94305; <sup>b</sup>Department of Chemistry, Technical University of Denmark, 2800 Kongens Lyngby, Denmark; <sup>c</sup>Japan Synchrotron Radiation Research Institute, Hyogo 679-5198, Japan; <sup>d</sup>Institute for Integrated Radiation and Nuclear Science, Kyoto University, Osaka 590-0494, Japan; and <sup>e</sup>Bioneer A/S, 2970 Hørsholm, Denmark

Edited by JoAnne Stubbe, Massachusetts Institute of Technology, Cambridge, MA, and approved January 26, 2021 (received for review October 26, 2020)

The pterin-dependent nonheme iron enzymes hydroxylate aromatic amino acids to perform the biosynthesis of neurotransmitters to maintain proper brain function. These enzymes activate oxygen using a pterin cofactor and an aromatic amino acid substrate bound to the Fe<sup>II</sup> active site to form a highly reactive Fe<sup>IV</sup> = O species that initiates substrate oxidation. In this study, using tryptophan hydroxylase, we have kinetically generated a pre-Fe<sup>IV</sup> = O intermediate and characterized its structure as a Fe<sup>II</sup>-peroxy-pterin species using absorption, Mössbauer, resonance Raman, and nuclear resonance vibrational spectroscopies. From parallel characterization of the pterin cofactor and tryptophan substrate-bound ternary Fe<sup>II</sup> active site before the O<sub>2</sub> reaction (including magnetic circular dichroism spectroscopy), these studies both experimentally define the mechanism of Fe<sup>IV</sup> = O formation and demonstrate that the carbonyl functional group on the pterin is directly coordinated to the Fe<sup>II</sup> site in both the ternary complex and the peroxy intermediate. Reaction coordinate calculations predict a 14 kcal/mol reduction in the oxygen activation barrier due to the direct binding of the pterin carbonyl to the Fe<sup>II</sup> site, as this interaction provides an orbital pathway for efficient electron transfer from the pterin cofactor to the iron center. This direct coordination of the pterin cofactor enables the biological function of the pterin-dependent hydroxylases and demonstrates a unified mechanism for oxygen activation by the cofactor-dependent nonheme iron enzymes.

oxygen activation | cofactor-dependent metalloenzymes | neurotransmitter biosynthesis

The mononuclear nonheme Fe<sup>II</sup> oxygen activating enzymes play important roles in many biological processes including antibiotic, natural product, and neurotransmitter biosynthesis; DNA and oxygen regulation; and bioremediation (1–9). These enzymes utilize a high-spin Fe<sup>II</sup> metal center bound by a conserved 2-His/1-carboxylate facial triad motif, which leaves three cis sites available for cofactor, substrate, and oxygen binding (10). In this broad class of enzymes, the  $\alpha$ -ketoglutarate ( $\alpha$ -KG)- and pterin-dependent enzymes use organic two-electron cofactors and Fe<sup>II</sup> active sites to reduce O<sub>2</sub> to form reactive Fe<sup>IV</sup> = O intermediates that initiate substrate oxidation (Scheme 1) (11). While the  $\alpha$ -KG-dependent enzymes have been more widely studied (12, 13), both of these enzyme subclasses utilize a general mechanistic strategy where the simultaneous binding of substrate and cofactor results in an open coordination position on the Fe<sup>II</sup> for the O<sub>2</sub> reaction (Scheme 1, *Left*) (14, 15).

The pterin-dependent hydroxylases (also called the aromatic amino acid hydroxylases) catalyze neurotransmitter biosynthesis and play critical roles in maintaining proper brain function (4). Phenylalanine hydroxylase (PAH) and tyrosine hydroxylase (TH) are part of the dopamine biosynthetic pathway, where PAH hydroxylates phenylalanine to tyrosine, which then gets converted to L-DOPA by TH. Similarly, tryptophan hydroxylase (TPH)

catalyzes the rate-limiting hydroxylation of tryptophan to 5-hydroxytryptophan, which then gets decarboxylated to form serotonin (4). Unlike the  $\alpha$ -KG cofactor, which binds directly to the Fe<sup>II</sup>, from spectroscopy and crystallography, the pterin cofactor is thought to bind in the active pocket, but not directly to the metal center (15–18). When the aromatic substrate binds in the active site pocket of the pterin-bound Fe<sup>II</sup> site, the pterin-dependent hydroxylases convert to five-coordinate (5C) sites that are primed for O<sub>2</sub> reactivity (Scheme 1, *Bottom*) (15, 16, 19).

Human TPH (hTPH) is found as a homotetramer, and each monomer has an N terminus regulatory domain, a catalytic domain, and a carboxyl terminus tetramerization domain. hTPH has two different isoforms: isoform 1 that catalyzes tryptophan degradation in peripheral parts of the human body and isoform 2, isolated more recently, that catalyzes serotonin biosynthesis in the brain (20). In this study, we have used the catalytic domain of TPH isoform 2 (referred to as TPH), as it is stable at higher concentrations (21), to determine the mechanism for pterin reduction of O<sub>2</sub>. We have defined the structure of the pterin- and tryptophan-bound ternary complex, evaluated its O<sub>2</sub> reactivity, and trapped and characterized the key intermediate in Fe<sup>IV</sup> = O formation. We have also computationally defined the mechanism by

## Significance

The mononuclear pterin-dependent nonheme iron enzymes catalyze the rate-limiting step in neurotransmitter biosynthesis and are essential in maintaining proper brain function. These enzymes utilize molecular oxygen, a redox active pterin cofactor, and a ferrous active site to generate an Fe<sup>IV</sup>-oxo intermediate that catalyzes substrate oxidation. This study demonstrates that the pterin cofactor directly coordinates to the iron center before oxygen activation and also coordinates to a kinetically generated peroxy-Fe<sup>II</sup> intermediate that is transiently observed in Fe<sup>IV</sup>-oxo formation. The direct coordination of the pterin cofactor to the iron center enables facile electron transfer to promote rapid oxygen reduction that facilitates the biological function of this family of enzymes and thus defines a unified oxygen activation mechanism for the cofactor-dependent nonheme iron enzymes.

Author contributions: S.R.I., K.D.T., and E.I.S. designed research; S.R.I., K.D.T., J.T.B., A.B.J., L.B.G., L.T.H., Y.Y., M.K., and S.K. performed research; Y.Y., M.K., S.K., M. Saito, M. Seto, H.E.M.C., and G.H.J.P. contributed new reagents/analytic tools; S.R.I., K.D.T., and E.I.S. analyzed data; and S.R.I. and E.I.S. wrote the paper.

The authors declare no competing interest.

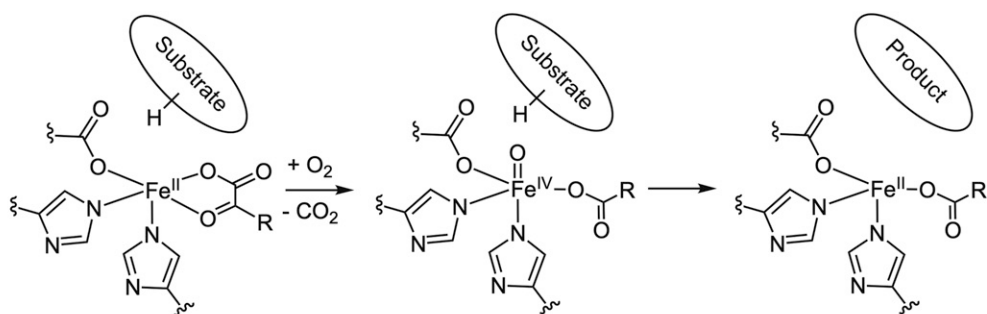
This article is a PNAS Direct Submission.

Published under the PNAS license.

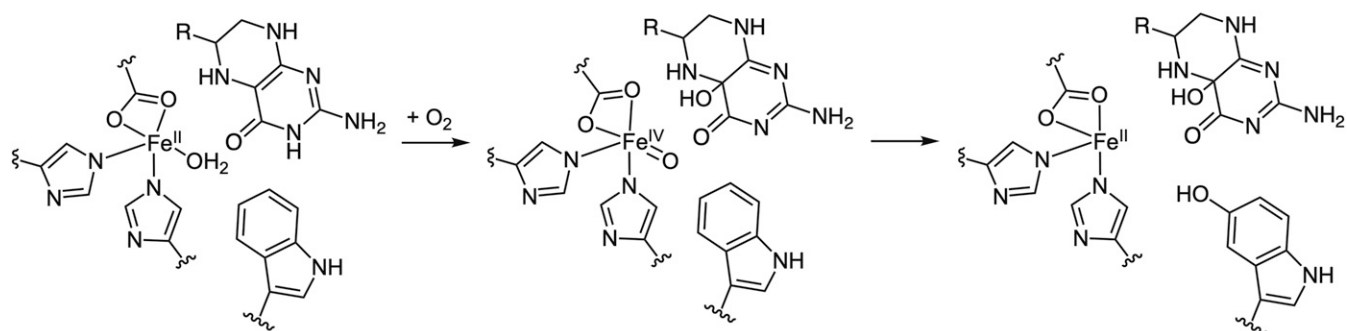
<sup>1</sup>To whom correspondence may be addressed. Email: solomone@stanford.edu.

This article contains supporting information online at <https://www.pnas.org/lookup/suppl/doi:10.1073/pnas.2022379118/-DCSupplemental>.

Published April 5, 2021.



## $\alpha$ KG-dependent Enzymes



## Pterin-dependent Enzymes

**Scheme 1.** (Top) Reaction mechanism for the  $\alpha$ -KG-dependent enzymes. (Bottom) Consensus mechanism (prior to this study) for the pterin-dependent enzymes.

which the pterin cofactor donates its two electrons for  $O_2$  activation with the low barrier required for its biological function.

### Results

**Spectroscopic Definition of the Ternary Complex.** From absorption spectroscopy (Fig. 1A, Top), addition of tryptophan (Trp) to the pterin ( $BH_4$ ) bound  $Fe^{II}$ -TPH site (forming the ternary complex) produces a new absorption feature at 330 nm ( $30,300\text{ cm}^{-1}$ ,  $\epsilon = 3,000\text{ M}^{-1} \cdot \text{cm}^{-1}$ ) that was previously observed in PAH (22). From low temperature magnetic circular dichroism (MCD) data (Fig. 1A, Bottom Inset), an excited state spectroscopy sensitive to the paramagnetic nature of the ground state at low temperature, substrate binding to the  $(Fe^{II}/BH_4)$ -TPH site also results in a large spectral change in the ligand field region with the appearance of a transition at  $\sim 5,000\text{ cm}^{-1}$ , indicating that the  $Fe^{II}$  has converted to a 5C site in this ternary complex (analysis in *SI Appendix, Defining Coordination Geometry Using Magnetic Circular Dichroism (MCD) Spectroscopy*). Extending the MCD data into the charge transfer region (Fig. 1A) shows that the  $\sim 30,000\text{ cm}^{-1}$  absorption band in the ternary complex has temperature-dependent intensity at 5 K (*SI Appendix, Fig. S1*), which requires that the paramagnetic  $Fe^{II}$  participate in this transition. Thus, this 330 nm absorption feature must involve a charge transfer between the  $Fe^{II}$  and either the pterin or tryptophan, as transitions involving the other first sphere ligands to the  $Fe^{II}$  do not contribute in this energy region (*SI Appendix, Fig. S2*). Although this absorption feature forms upon tryptophan addition to the  $(Fe^{II}/BH_4)$ -TPH site, tryptophan cannot coordinate to the  $Fe^{II}$  and perform productive chemistry because of the lack of a heteroatom oriented toward the  $Fe^{II}$  center. On the other hand, the carbonyl functional group of the reduced pterin cofactor can directly bind to the  $Fe^{II}$  center to produce the high absorption intensity of this charge transfer.

From time-dependent (TD) density functional theory (DFT) calculations (*SI Appendix, Figs. S3–S6*), the  $30,000\text{ cm}^{-1}$  absorption

feature is assigned as a ligand-to-metal charge transfer (LMCT), which is a transition between the  $\pi$  HOMO (highest occupied molecular orbital) of the reduced pterin and a  $d\pi^*$  orbital on the  $Fe^{II}$ . DFT calculations on the one electron oxidized pterin cofactor result in structural distortions along the carbonyl ( $C=O$ ) and  $C4\alpha-N5$  bonds (*SI Appendix, Figs. S7 and S8*) that would be

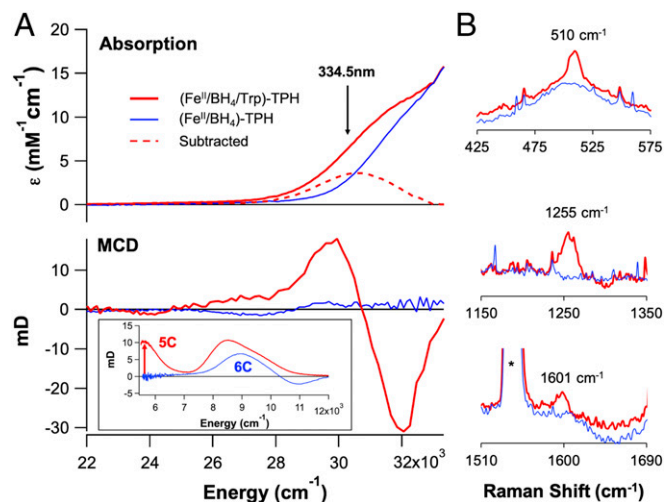


**Fig. 1.** (A) Absorption (Top) and 7 T, 5 K MCD (Bottom) spectra for pterin-bound  $Fe^{II}$ -TPH (125  $\mu$ M, blue) and pterin- and tryptophan-bound ternary  $Fe^{II}$ -TPH (125  $\mu$ M, red). (Inset, Bottom) Near-infrared MCD spectra demonstrating the formation of a 5C site upon tryptophan binding (red) to the  $(Fe^{II}/BH_4)$ -Trp active site. (B) Resonance Raman data collected at 334.5 nm (arrow in A) showing resonance enhancement of three vibrations upon tryptophan binding (0.5 mM, red) to the  $(Fe^{II}/BH_4)$ -TPH active site (0.5 mM, blue).

present in resonance Raman spectroscopy, which is a technique that probes the vibrations associated with metal–ligand distortions of the charge transfer transition leading to resonance enhancement. Several resonance enhanced features are observed in the resonance Raman data collected on the ternary complex ( $\lambda_{\text{ex}} = 334.5$  nm, Fig. 1B and *SI Appendix*, Fig. S9), where the highest energy vibration at  $1,601\text{ cm}^{-1}$  is  $94\text{ cm}^{-1}$  lower than the corresponding vibration observed for reduced pterin cofactor, which has its carbonyl stretch at  $1,695\text{ cm}^{-1}$  (23). From frequency calculations on the pterin-bound ternary complex, the direct coordination of the pterin through its carbonyl functional group elongates the C–O bond by  $0.037\text{ \AA}$ , which results in a reduction of the C = O stretching frequency by  $63\text{ cm}^{-1}$  (*SI Appendix*, Table S1) that reproduces the experimental Raman data. While there were early reports that suggested a metal–pterin interaction from spectroscopic studies on  $\text{Cu}^{\text{II}}$ -PAH (24, 25) and the ternary complex in PAH (26), the subsequent crystal structures of the ternary complex of PAH in 2002 showed no pterin coordination (18, 19, 27), and since then, it has been generally thought that the pterin cofactor does not bind directly to the iron in the pterin-dependent hydroxylases. Here, our spectroscopic data have defined the direct coordination of the pterin cofactor through its carbonyl functional group to the  $\text{Fe}^{\text{II}}$  ternary active site before  $\text{O}_2$  reactivity.

**$\text{O}_2$  Reaction with Ternary Complex: Formation and Decay of a Pre- $\text{Fe}^{\text{IV}} = \text{O}$  Intermediate.** The single turnover reaction of  $\text{O}_2$  with  $(\text{Fe}^{\text{II}}/\text{BH}_4/\text{Trp})$ -TPH (with stoichiometric amounts of  $\text{BH}_4$  and Trp) was monitored by stopped-flow absorption spectroscopy. The results from this reaction in  $\text{D}_2\text{O}$ /sucrose buffer are

presented below as it enables the maximal accumulation of an intermediate species (reactions were performed in both  $\text{H}_2\text{O}$  and  $\text{D}_2\text{O}$  and with and without 20 weight/volume% sucrose added to the reaction buffer). From Fig. 2A, the decay of the 330 nm ternary complex LMCT leads to the formation of a new absorption feature at 442 nm within the first 175 ms of the reaction, which decays within 2 s (Fig. 2B). The decay of this species is concomitant with the growth of an absorption feature at 248 nm (Fig. 2C, green), which corresponds to the formation of hydroxybiopterin (hydrolyzed to quinonoid dihydrobiopterin at long times as shown in *SI Appendix*, Fig. S10) (28). The formation of hydroxybiopterin is the marker for the corresponding formation of an  $\text{Fe}^{\text{IV}} = \text{O}$  species, indicating that the O–O bond of  $\text{O}_2$  is cleaved in this stage of the reaction. Thus, the 442 nm absorption feature is associated with a pre- $\text{Fe}^{\text{IV}} = \text{O}$  intermediate and is similar to a previously observed transient signal in another isozyyme of TPH (29).

To probe the mechanism of formation and decay of the 442 nm intermediate, its  $\text{O}_2$  dependence and H/D solvent kinetic isotope effect (KIE) were evaluated. In Fig. 2D, the formation of the intermediate is dependent on the concentration of  $\text{O}_2$  and is approaching saturation at the highest oxygen concentration (1 mM), requiring an  $\text{O}_2$  equilibrium binding step. Furthermore, in deuterated buffer, the absorption maximum is higher and occurs at longer time (Fig. 2E), reflecting a normal KIE on the decay of the intermediate but no KIE on its formation. Additionally, the decay of this species has a fast phase and a slow phase (*SI Appendix*, Fig. S11, purple and green lines), which cannot be simply fitted as two decay pathways for the intermediate since it does not capture the biphasic behavior of the absorption time

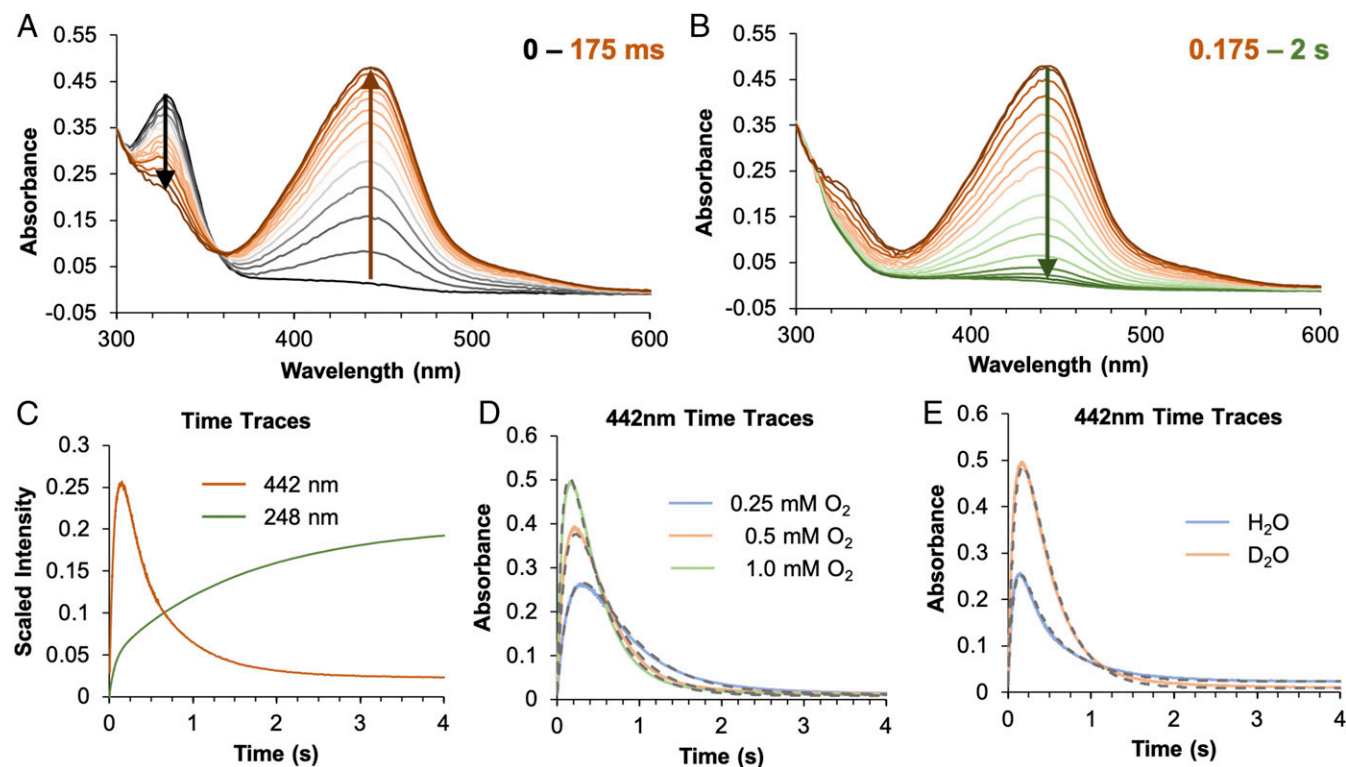


Fig. 2. Stopped-flow absorption spectra monitoring the reaction of  $0.15\text{ mM } (\text{Fe}^{\text{II}}/\text{BH}_4/\text{Trp})$ -TPH with  $1\text{ mM } \text{O}_2$  in  $\text{Hepes}/(\text{NH}_4)_2\text{SO}_4/\text{sucrose}$  buffer (pD 7) showing (A) the disappearance of an absorption at  $330\text{ nm}$  (black arrow) and the growth of an absorption feature at  $442\text{ nm}$  (brown arrow) in the first  $175\text{ ms}$  and (B) its subsequent decay (green arrow) within  $2\text{ s}$ . (C) Monitoring the reaction of  $0.125\text{ mM } (\text{Fe}^{\text{II}}/\text{BH}_4/\text{Trp})$ -TPH in  $\text{Hepes}/(\text{NH}_4)_2\text{SO}_4$  (pH 7) with  $1\text{ mM } \text{O}_2$  at  $442\text{ nm}$  (orange, with sucrose added) and  $248\text{ nm}$  (green, without added sucrose). (D) Monitoring the reaction of  $0.15\text{ mM } (\text{Fe}^{\text{II}}/\text{BH}_4/\text{Trp})$ -TPH in  $\text{Hepes}/(\text{NH}_4)_2\text{SO}_4/\text{sucrose}$  buffer (pD 7) with  $0.25\text{ mM } \text{O}_2$  (blue),  $0.5\text{ mM } \text{O}_2$  (orange), and  $1.0\text{ mM } \text{O}_2$  (green) at  $442\text{ nm}$ . These time traces were fitted (gray dashes) with the kinetic model presented in Scheme 2. (E) Monitoring the reaction of  $(\text{Fe}^{\text{II}}/\text{BH}_4/\text{Trp})$ -TPH with  $1\text{ mM } \text{O}_2$  in  $\text{Hepes}/(\text{NH}_4)_2\text{SO}_4/\text{sucrose}$  buffer at pH 7 (blue,  $0.125\text{ mM}$  protein) and pD 7 (orange,  $0.15\text{ mM}$  protein) at  $442\text{ nm}$ . These time traces are fitted with the kinetic model presented in Scheme 2, and enlarged fits of both the  $\text{H}_2\text{O}$  and  $\text{D}_2\text{O}$   $\text{O}_2$ -dependent data are shown in *SI Appendix*, Fig. S13.

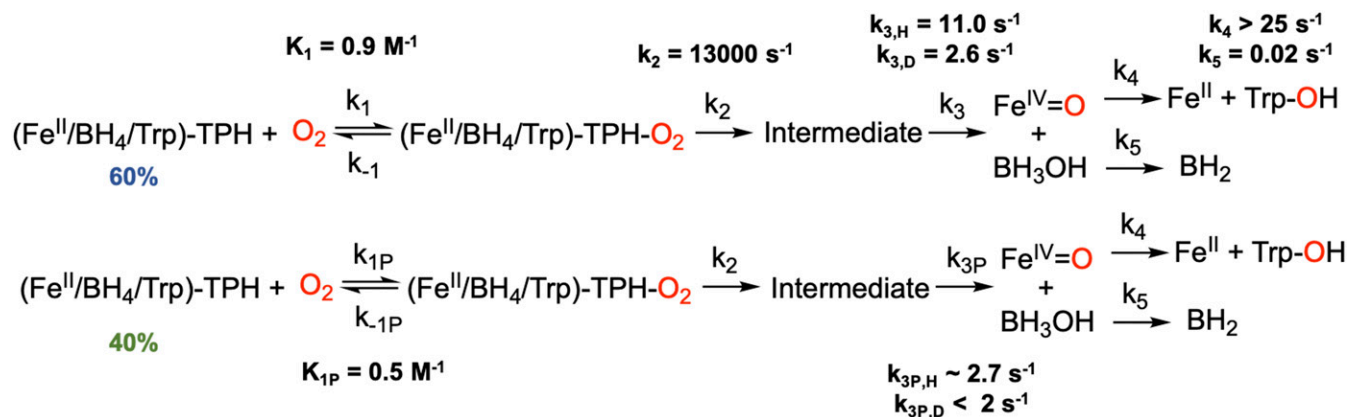
trace between 0.6 and 2 s (*SI Appendix*, Fig. S11, green line). To capture this biphasic decay, the formation of the intermediate requires two parallel reactions with two O<sub>2</sub> binding equilibria (with the same ternary-O<sub>2</sub> decay rate, k<sub>2</sub> in Scheme 2). This kinetic behavior is interpreted to reflect the differential O<sub>2</sub> reactivity of the two ternary 5C sites observed in the MCD data (Fig. 1A) for the ternary Fe<sup>II</sup> complex (as described in *SI Appendix*, Fig. S12 and associated text). Fitting the kinetic data in Fig. 2D and *SI Appendix*, Fig. S13 to the model in Scheme 2 that includes two O<sub>2</sub> binding equilibria [with the 60/40 speciation of the ternary Fe<sup>II</sup> site from Mössbauer spectroscopy (Fig. 3A)], the absorption feature of the 442 nm intermediate has a molar extinction coefficient of 5,500 M<sup>-1</sup> cm<sup>-1</sup>, the fast decay phase has a normal KIE of 4.2 (k<sub>3</sub> in Scheme 2, *Top*), and the slow decay phase (k<sub>3P</sub>) also has a normal KIE but is too small to accurately estimate. Importantly, the fast rate of formation (k<sub>2</sub>) and slow decay (especially in D<sub>2</sub>O, k<sub>3</sub>) enables accumulation of this intermediate for spectroscopic characterization.

**Spectroscopic Definition of the Pre-Fe<sup>IV</sup> = O Intermediate.** The oxidation state of the pre-Fe<sup>IV</sup> = O intermediate was characterized using Mössbauer spectroscopy, which is a nuclear absorption technique sensitive to the electron density at and around an <sup>57</sup>Fe nucleus. Compared to the ternary Fe<sup>II</sup> site (Fig. 3A), a new quadrupole doublet (Fig. 3B, purple) appears with a similar isomer shift (δ = 1.25 mm/s) but a smaller quadrupole splitting (ΔE<sub>Q</sub> = 2.80 mm/s), defining it as an Fe<sup>II</sup> species. The formation of the 442 nm absorption feature occurs with the decay of the 330 nm pterin-to-Fe<sup>II</sup> charge transfer in the ternary complex, which is indicative of pterin oxidation upon reaction with O<sub>2</sub>. Since, from Mössbauer, the intermediate is Fe<sup>II</sup> and its decay leads to the formation of an Fe<sup>IV</sup> = O, this intermediate can be formulated as either an Fe<sup>II</sup>-superoxide/BH<sub>4</sub><sup>•+</sup> (or BH<sub>3</sub><sup>•</sup>) or an Fe<sup>II</sup>-peroxy/oxidized pterin species. The absorption spectra of BH<sub>4</sub><sup>•+</sup> and BH<sub>3</sub><sup>•</sup> do not reproduce the absorption spectrum in Fig. 2A (30, 31) and thus indicate that this species is an Fe<sup>II</sup>-peroxy/oxidized pterin intermediate.

The Fe<sup>II</sup>-peroxy/oxidized pterin intermediate can either maintain or lose the bond between the Fe<sup>II</sup> and the pterin carbonyl present in the ternary Fe<sup>II</sup> site (*SI Appendix*, Figs. S14 and S15 for structural comparison). TD-DFT calculations show that, for both cases, the lowest energy absorption transition is a metal-to-ligand charge transfer (MLCT) into the oxidized pterin π orbital, with the more intense transition predicted for the carbonyl bound structure because of direct orbital overlap (*SI Appendix*, Figs. S16 and S17). This assignment is confirmed by

resonance Raman spectroscopy (Fig. 3C and *SI Appendix*, Figs. S18 and S19 for resonance enhancement) in the metal–ligand region between 400 and 800 cm<sup>-1</sup>, as the resonance enhanced vibrations at 451, 489, and 792 cm<sup>-1</sup> only have modest isotope shifts upon <sup>18</sup>O<sub>2</sub> substitution. DFT calculations for the one electron reduction of a peroxy oxidized pterin (resulting from the MLCT) predict structural distortions that contribute to the resonance enhancement along the carbonyl C = O and the pyrazine ring C<sub>8</sub>-N<sub>8α</sub> bonds (*SI Appendix*, Fig. S20). From the resonance Raman data in the intrapterin region above 1,000 cm<sup>-1</sup> (Fig. 3C, *Inset* and *SI Appendix*, Figs. S18 and S19 for resonance enhancement), the highest energy vibration at 1,570 cm<sup>-1</sup> is 110 cm<sup>-1</sup> lower relative to the carbonyl stretch (1,680 cm<sup>-1</sup>) of an oxidized pterin (23). Frequency calculations on computational models with and without the pterin carbonyl bound to the peroxy-Fe<sup>II</sup> intermediate demonstrate that, as in the ternary complex, carbonyl binding leads to a ~100 cm<sup>-1</sup> decrease in the C = O stretching frequency (*SI Appendix*, text below *SI Appendix*, Fig. S20 and Table S2 for detailed peak assignment), reproducing the experimental data. Additionally, these calculations also assign the vibrations in the metal–ligand region, where the most intense vibration at 489 cm<sup>-1</sup> is the Fe-O<sub>carbonyl</sub> stretch, while the 451 cm<sup>-1</sup> feature is the Fe-O<sub>peroxy</sub> stretch (*SI Appendix*, Table S2 and Fig. S21). The modest <sup>18</sup>O<sub>2</sub> isotope shift of the Fe-O<sub>peroxy</sub> stretch (Δ = 5 cm<sup>-1</sup>) is due to its distribution into a number of stretching and bending modes associated with the formation of a six-membered ring. This derives from the simultaneous coordination of the pterin carbonyl and peroxide, thus defining the geometric structure of the peroxy-Fe<sup>II</sup> intermediate (Fig. 3F).

The electronic and geometric structures of the Fe<sup>II</sup> ternary complex and the peroxy intermediate were further investigated using nuclear resonance vibrational spectroscopy (NRVS). NRVS measures the vibrational sidebands of the <sup>57</sup>Fe nuclear Mössbauer transition where the spectral intensity gives the Fe motion in a normal mode at the observed energy. Thus, this technique is sensitive to changes in ligation around an <sup>57</sup>Fe center. In Fig. 3D, *Top*, the NRVS spectrum of the ternary complex (black) has been overlaid with the spectrum of the intermediate (red). The NRVS data on the ternary complex (black) and peroxy intermediate (red) show a redistribution of intensity from 230 and 260 cm<sup>-1</sup> (black arrow) to 200 to 220 cm<sup>-1</sup>, 240 cm<sup>-1</sup>, and 325 cm<sup>-1</sup> (red arrows). In order to interpret the changes in the NRVS data, we employed an NRVS/DFT methodology to reproduce the vibrational changes in the experimental data that has been previously used to characterize Fe<sup>IV</sup> = O, Fe<sup>III</sup>-peroxy and Fe<sup>III</sup>-superoxy intermediates (32–34). The simulations (Fig. 3D, *Bottom*) for the ternary complex, with



**Scheme 2.** Kinetic model for the formation and decay of the O<sub>2</sub>-dependent intermediate observed at 442 nm in stopped-flow absorption spectroscopy. The details of how this model was developed are presented in the *SI Appendix*. From spectroscopy, 60% of the reaction occurs through the top pathway, and 40% occurs through the bottom pathway. The kinetic rate constants and equilibrium constants that fit the data are given for each pathway.

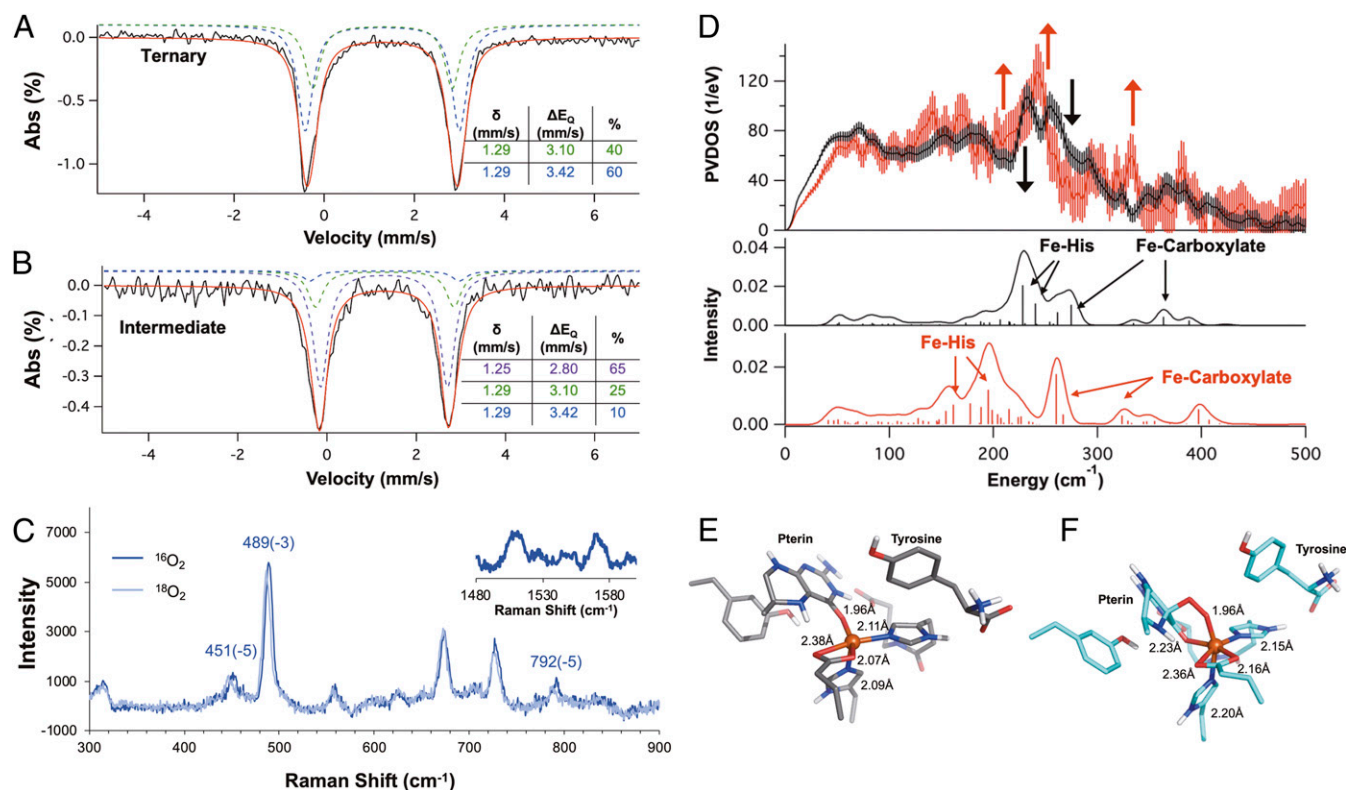


**Fig. 3.** Mössbauer spectra of the (A) ternary complex and (B) the 442 nm pre- $\text{Fe}^{\text{IV}} = \text{O}$  intermediate generated by reacting 0.5 mM ( $\text{Fe}^{\text{II}}/\text{BH}_4/\text{Trp}$ )-TPH with 1 mM  $\text{O}_2$  in HEPES/ $(\text{NH}_4)_2\text{SO}_4$ /sucrose buffer (pD 7). The parameters for the ternary complex and the intermediate are listed in their respective tables. (C) Resonance Raman spectra using the 457.9 nm laser line of the 442 nm intermediate (0.5 mM ( $\text{Fe}^{\text{II}}/\text{BH}_4/\text{Trp}$ )-TPH + 1 mM  $\text{O}_2$ ) rapid-freeze quenched at 150 ms. (Inset) Raman shifts measured in the 1,480 to 1,610  $\text{cm}^{-1}$  region showing resonance enhanced features at 1,514 and 1,570  $\text{cm}^{-1}$ . The change in the energies of the vibrations from the  $^{16}\text{O}_2/^{18}\text{O}_2$  isotope perturbation are indicated. Note that the 1,514 and 1,570  $\text{cm}^{-1}$  features do not show an  $\text{O}_2$  isotope effect. (D, Top) NRVs spectra of the ternary  $\text{Fe}^{\text{II}}$  complex (black) and the rapid freeze quenched intermediate (red, 1 mM ( $\text{Fe}^{\text{II}}/\text{BH}_4/\text{Trp}$ )-TPH + 1 mM  $\text{O}_2$ ). The error bars in the processed spectra are represented by vertical lines. The contribution of the ternary complex to the intermediate spectrum was removed and the spectrum renormalized as described in *SI Appendix, Fig. S22*. The black arrow depicts loss of intensity, while the red arrows show gain in intensity going from the ternary  $\text{Fe}^{\text{II}}$  complex to the intermediate spectrum. (Bottom) Simulation of NRVs spectra of the ternary complex (black) and the peroxy intermediate (red) with the pterin carbonyl bound to the  $\text{Fe}^{\text{II}}$  center. Optimized structures of (E) the ternary complex and the (F) peroxy intermediate with the pterin carbonyl bound. The metal–ligand distances are indicated.

the pterin carbonyl bound to the iron center (black) show two Fe–His modes at 228 and 241  $\text{cm}^{-1}$  as well as two Fe–carboxylate modes at 275 and 364  $\text{cm}^{-1}$ . Going from the ternary complex to the peroxide intermediate with the carbonyl bound to the  $\text{Fe}^{\text{II}}$  (red), the Fe–His modes shift to 160 and 195  $\text{cm}^{-1}$  (lower in energy by 68 and 46  $\text{cm}^{-1}$ , respectively) and the Fe–carboxylate modes shift to 260 and 322  $\text{cm}^{-1}$  (lower in energy by 15 and 42  $\text{cm}^{-1}$ , respectively). In the calculations, these energy decreases reflect elongation of the Fe–His and Fe–carboxylate bonds in going from the 5C ternary site to the 6-coordinate (6C) intermediate due to the coordination of an anionic peroxide ligand (as shown in Fig. 3 E and F). These simulations reproduce the experimental data as the gain in intensity in the peroxo NRVs spectrum at 200 to 220  $\text{cm}^{-1}$  is due to the Fe–His modes shifting down in energy and at 240 and 325  $\text{cm}^{-1}$  are due to the Fe–carboxylate modes shifting to lower energy. Additionally, the loss of intensity at 260  $\text{cm}^{-1}$  going from the ternary complex to the peroxo intermediate is captured by the decrease in calculated energy of the Fe–carboxylate mode from 275 to 260  $\text{cm}^{-1}$ . Note that while there is a discrepancy in the absolute energy values of the calculated spectra relative to the experimental data, the trends in intensity going from the ternary to the peroxo complex are internally consistent. On the other hand, the active site models without the pterin carbonyl bound do not reproduce the experimental changes observed in the NRVs data (*SI Appendix*, see description with *SI Appendix, Fig. S23*). Thus, the NRVs data complement the resonance Raman data on both the

ternary site and peroxo intermediate and demonstrate the direct coordination of the pterin carbonyl with the  $\text{Fe}^{\text{II}}$  in both structures.

#### **$\text{O}_2$ Reaction Coordinate: Role of Direct Coordination of Pterin to $\text{Fe}^{\text{II}}$ .**

To evaluate the impact of direct pterin coordination on oxygen activation, we have calculated the reaction coordinates of two 5C ternary complexes (*SI Appendix, Fig. S4*), one with and one without the pterin carbonyl bound to the metal center (Fig. 4). When the pterin carbonyl is bound,  $\text{O}_2$  binds to the open coordination site on the  $\text{Fe}^{\text{II}}$  to form a superoxide species that is only uphill by 1.4 kcal/mol (Fig. 4A, green). In contrast, when the pterin is not bound to  $\text{Fe}^{\text{II}}$ ,  $\text{O}_2$  binding is uphill by 11.7 kcal/mol (Fig. 4A, red), comparable to other nonheme iron enzyme calculations (34, 35). The superoxide then forms the peroxide species through the attack of its distal O (relative to Fe) on the C4 $\alpha$  position of the pterin cofactor along with a proton transfer from the  $\text{N}_3$  amine on the pterin to a nearby carboxylate residue (Fig. 4B, right circled). When the pterin carbonyl is bound, the formation of the peroxo intermediate from the superoxo has a calculated reaction barrier of 5.6 kcal/mol (Fig. 4A and *SI Appendix, Fig. S24*), compared to the  $\sim 10$  kcal/mol barrier estimated (based on the two-dimensional potential energy surface, *SI Appendix, Fig. S25*) when the pterin carbonyl is not bound. Thus, comparing the reaction coordinates with and without pterin carbonyl bound to  $\text{Fe}^{\text{II}}$ , the direct binding of the pterin to the

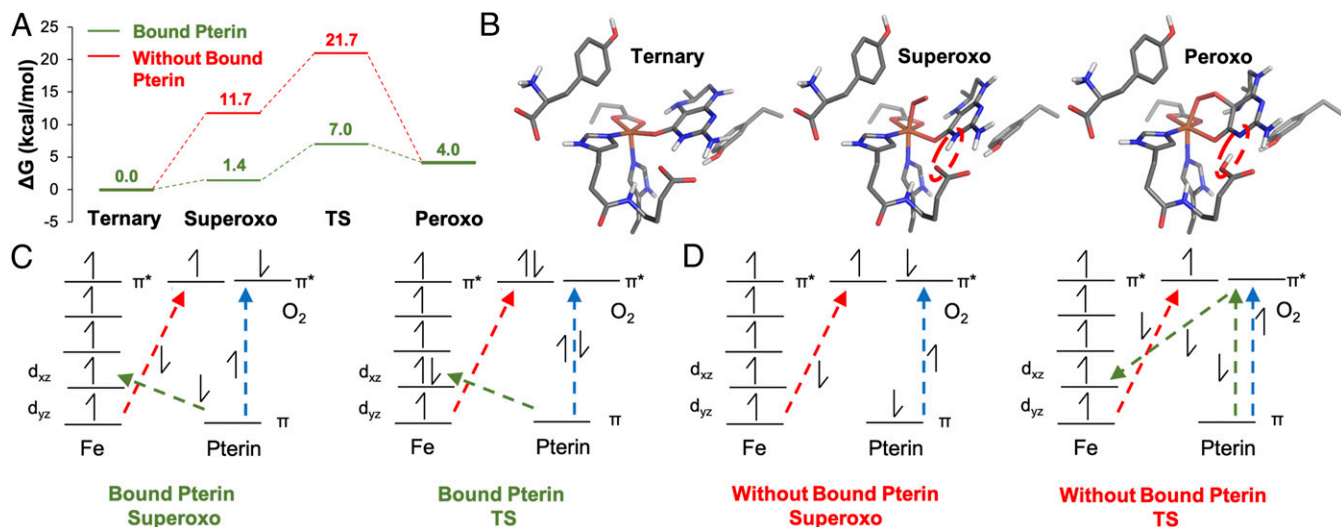


**Fig. 4.** (A)  $O_2$  activation reaction coordinate of the ternary complex with pterin carbonyl bound to  $Fe^{II}$  (green) and without the pterin carbonyl bound to  $Fe^{II}$  (red). (B) The geometries for the ternary, superoxo, and peroxy complexes in the reaction coordinate with the pterin carbonyl bound. The red dashed ovals demonstrate the proton transfer from the pterin cofactor to a nearby carboxylate residue. (C and D) Qualitative electronic structures and electron transfer pathways for the superoxo and TS structures for (C) the reaction coordinate with the pterin carbonyl bound and (D) the reaction coordinate without the pterin carbonyl bound to  $Fe^{II}$ .

$Fe^{II}$  center reduces the barrier for  $O_2$  activation by 14.7 kcal/mol (Fig. 4A), which corresponds to an  $\sim 10^{10}$  increase in kinetic rate.

To understand the origin of this reduction in barrier, the changes in electronic structures along each reaction coordinate were assessed and compared. Before the  $O_2$  reaction, the pterin carbonyl-bound ternary complex donates electron density to the Fe center stabilizing the ternary complex by  $\sim 8$  kcal/mol (SI Appendix, Figs. S26 and S27). This electron donation corresponds to the LMCT observed in the absorption spectrum for the ternary complex in Fig. 1A at  $\sim 30,000\text{ cm}^{-1}$  and plays a key role in  $O_2$  activation. The electronic structures of the superoxide species in Fig. 4C and D (formally high-spin  $Fe(III)$  [ $\alpha$ -spins] antiferromagnetically coupled to  $O_2^{\bullet -}$  ( $\beta$  spin) to give  $S_{Tot} = 2$ ; see SI Appendix, Figs. S28 and S29 for septet versus quintet) with and without pterin bound demonstrate that there is  $\beta$  electron transfer from the Fe to  $O_2$  (red arrow) and  $\alpha$  electron transfer from the pterin to the  $O_2$  moiety (blue arrow in Fig. 4C and D and SI Appendix, Figs. S30 and S31). However, when the pterin carbonyl is bound to the  $Fe^{II}$ , there is additional direct donation of electron density from the pterin cofactor to the iron center (green arrow) that results in the  $\sim 10$  kcal/mol stabilization of  $O_2$  binding relative to superoxo formation without bound pterin. From the bound superoxo species, formation of the peroxy intermediate completes the three-electron transfer processes shown in Fig. 4C and D (red, blue, and green arrows). When the pterin carbonyl is bound, the electronic structure of the transition state for peroxy formation (Fig. 4C and SI Appendix, Figs. S32 and S33) reveals that the electron transfer processes between the Fe and  $O_2$  (red arrow) and the pterin and Fe (green arrow) are far along. However, when the pterin carbonyl is not bound, the lack of direct overlap between the pterin and iron requires that this electron transfer be mediated by  $O_2$ . From Fig. 4D TS, this process involves the concerted electron transfer from the  $O_2\ \pi^*$  to Fe  $d_{xz}$  and from the pterin  $\pi$  to  $O_2\ \pi^*$  (SI Appendix, Figs. S34 and S35). In a transition state-like structure for the reaction coordinate without pterin carbonyl bound (PES in SI Appendix, Fig. S25), the electron transfer from the iron to the  $O_2$  is far along, but there is only partial electron transfer from the pterin ( $\beta$ ) to the iron (Fig. 4D TS, green arrows). Thus, relative to the electronic structure of the transition state with the

pterin carbonyl bound, the lack of carbonyl binding results in less total electron transfer and increases the barrier for superoxo to peroxy formation by 5 kcal/mol (Fig. 4A). Thus, the direct donation from the pterin cofactor to the  $Fe^{II}$  through its carbonyl leads to more favorable  $O_2$  binding and efficient electron transfer, which collectively result in the 14 kcal/mol lower reaction barrier.

## Discussion

In this study, we have defined the geometric and electronic structures of the pterin- and tryptophan-bound  $Fe^{II}$ -TPH active site and the  $Fe^{II}$ -peroxy-pterin intermediate and the reaction mechanism through which the pterin cofactor provides its two electrons for  $O_2$  activation. When both pterin and tryptophan are bound to  $Fe^{II}$ -TPH, we observe a new absorption feature at 330 nm, which is not present when only pterin is bound to the  $Fe^{II}$  site. The 330 nm absorption feature is paramagnetic from MCD spectroscopy, which establishes that the charge transfer involves

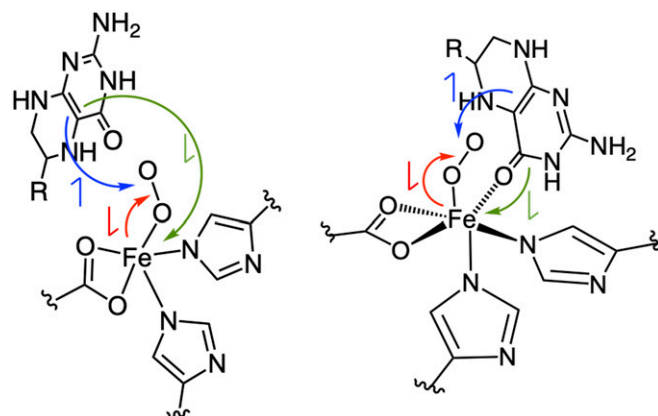
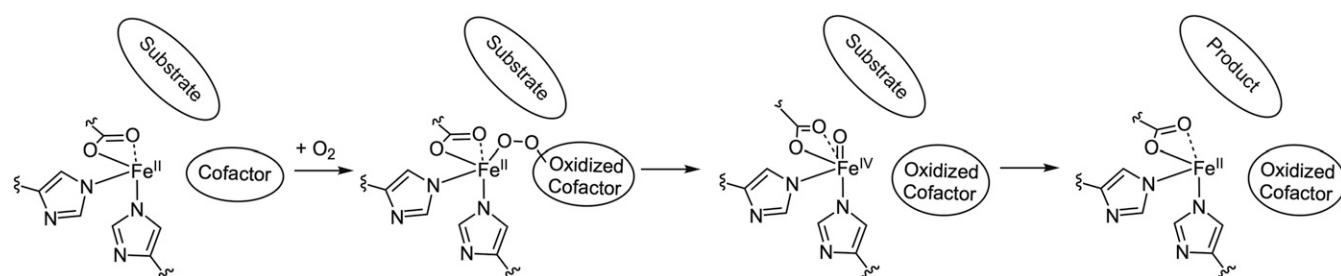


**Fig. 5.** Comparison of the Fe-superoxo structures without (Left) and with (Right) the pterin carbonyl bound. The red arrows represent electron transfer from the iron to  $O_2$ , the blue arrows represent electron transfer from the pterin to  $O_2$ , and the green arrows represent electron transfer from the pterin to the iron center.



**Scheme 3.** Mechanism for the cofactor-dependent enzymes defined by this study. Both the pterin and  $\alpha$ -KG cofactors bind to the metal center in the ternary complex and react with  $O_2$  to form peroxy intermediate that undergoes heterolytic O–O bond cleavage to form  $Fe^{IV} = O$  intermediates that catalyze substrate oxidation.

the  $Fe^{II}$ . Additionally, the resonance Raman spectrum associated with the 330 nm band reveals a direct interaction between the pterin carbonyl and the metal center based on the presence of a carbonyl stretch, which decreases from  $1,695\text{ cm}^{-1}$  in a reduced pterin cofactor to  $1,601\text{ cm}^{-1}$  in the pterin and tryptophan bound ternary complex. Reaction of this ternary complex with  $O_2$  generates a 442 nm absorption feature associated with an  $Fe^{II}$ -peroxy-pterin intermediate. The 442 nm band is a metal-to-pterin charge transfer transition based on the lack of a resonance-enhanced O–O stretching vibration and the presence of intrapterin stretches in the resonance Raman spectrum associated with this band. Furthermore, the highest energy resonance-enhanced features are more than  $100\text{ cm}^{-1}$  lower than the carbonyl stretch for an oxidized pterin cofactor ( $1,680\text{ cm}^{-1}$ ), which demonstrates that the pterin carbonyl is also directly bound to the iron center in the peroxy-bridged intermediate.

By computationally evaluating the  $O_2$  reaction coordinate with and without carbonyl bound to the iron center, we calculate a 14 kcal/mol lower reaction barrier with the pterin bound, which corresponds to a  $10^{10}$ -fold increase in reaction rate. When the pterin is not bound to the  $Fe^{II}$  center,  $O_2$  first binds, the iron is partially oxidized to  $Fe^{III}$ , and the  $O_2$  is partially reduced to superoxide, which is 10 kcal/mol uphill. In going from the superoxy to the peroxy species, the pterin cofactor needs to transfer one electron to the  $O_2$  and one electron to the iron center to form the  $Fe^{II}$ -peroxy oxidized pterin (Fig. 5, *Left*). While the electron transfer from the pterin to the  $O_2$  is straightforward (Fig. 5, blue arrow), the second electron transfer from the pterin to the  $d\pi$  orbital on the iron center needs to proceed through one of the superoxide  $\pi^*$  molecular orbitals (green arrow). The lack of direct orbital overlap between the pterin and iron makes this electron transfer less efficient, which gives rise to the high reaction barrier. On the other hand, when the pterin carbonyl is bound to the metal center,  $O_2$  binding is thermoneutral due to donation from the pterin to the metal center that compensates the electron transfer from iron to  $O_2$  as there is direct orbital overlap between the pterin  $\pi$  HOMO and  $d\pi^*$  orbital (Fig. 5, *Right*, green arrow), which results in a much lower reaction barrier. In the pterin-dependent hydroxylases, under turnover conditions, product dissociation is the rate-limiting step and has a barrier of  $\sim 16$  kcal/mol (based on a rate constant of  $0.1$  to  $1\text{ s}^{-1}$ ) (22, 29, 36, 37). When carbonyl is not bound to the iron center, the overall calculated turnover barrier of  $>21$  kcal/mol would result in  $\sim 10^4$ -fold slower turnover. This barrier would be similar to that of uncoupled turnover (oxidation of pterin cofactor, but not substrate) (24, 38), which would result in enzymatic dysregulation and impact key metabolic pathways necessary for proper brain function. As the pterin-dependent hydroxylases catalyze the rate-limiting steps in dopamine and

serotonin biosynthesis as well as aromatic amino acid degradation, impairment of their reactivity has been linked to neurological diseases such as phenylketonuria (PAH), Parkinson's, schizophrenia (TH) and depressive disorders (TPH), highlighting the importance of their coupled reactivity.

Finally, this study defines a unifying mechanism employed by the cofactor-dependent iron enzymes to enable rapid  $O_2$  activation (Scheme 3). For both the pterin and  $\alpha$ -KG-dependent nonheme iron enzymes, both the cofactor and substrate must simultaneously bind to open a coordination position on the  $Fe^{II}$ , which enables  $O_2$  activation. In the  $\alpha$ -KG-dependent nonheme iron enzymes, substrate coordination to the  $Fe^{II}/\alpha$ KG site induces formation of the 5C site needed for  $O_2$  activation. For the pterin-dependent hydroxylases, binding of the substrate causes both the pterin to bind to the iron and also opens a coordination position for  $O_2$  activation. Both enzyme classes thus prevent uncoupled reactivity (i.e.,  $O_2$  activation without substrate oxidation) and autooxidation when only the cofactor is bound to the enzyme—the  $\alpha$ -KG-dependent enzymes by keeping the site 6C and the pterin-dependent enzymes by cofactor binding to the  $Fe^{II}$  only in the presence of substrate.  $O_2$  binding results in some electron transfer from the iron to the  $O_2$  (i.e.,  $Fe^{III}$ -superoxo character), which then requires the cofactor to donate two electrons (one to  $O_2$  and one to Fe) to generate the peroxy-bound  $Fe^{II}$  intermediate observed here and proposed to form in the  $\alpha$ -KG-dependent enzymes (35, 39, 40). The peroxy- $Fe^{II}$  species then undergoes a two-electron reductive cleavage of the O–O bond to form the  $Fe^{IV} = O$  intermediate, primed to initiate substrate chemistry. We have demonstrated that for both subclasses, electron transfer from the cofactor to the iron requires orbital overlap and thus the direct coordination of the cofactor to the  $Fe^{II}$ . Without the cofactor binding to the iron, the oxygen reaction would be too slow for metabolic function.

## Materials and Methods

Details about protein expression and purification, sample preparation, spectroscopic methods, stopped-flow absorption experiments, and computational methods are provided in *SI Appendix, Materials and Methods*.

**Data Availability.** All study data are included in the article and/or supporting information.

**ACKNOWLEDGMENTS.** This research was supported by US NIH Grants GM 40392 (to E.I.S., S.R.L., J.T.B., and A.B.J.) and F32GM122194 (to L.B.G.) and Independent Research Fund Denmark Grant DFF-6108-00247 (to H.E.M.C. and G.H.J.P.). K.D.T. acknowledges financial support via an Academic Excellence Scholarship from the Department of Chemistry, Technical University of Denmark. The synchrotron experiments were performed at SPring-8 with the approval of the Japan Synchrotron Radiation Research Institute (proposal nos. 2017B0137, 2018A0137, and 2018B0137).

1. J. E. Baldwin, E. Abraham, The biosynthesis of penicillins and cephalosporins. *Nat. Prod. Rep.* **5**, 129–145 (1988).
2. F. H. Vaillancourt, J. Yin, C. T. Walsh, SyrB2 in syringomycin E biosynthesis is a non-heme  $Fe^{II}$   $\alpha$ -ketoglutarate- and  $O_2$ -dependent halogenase. *Proc. Natl. Acad. Sci. U.S.A.* **102**, 10111–10116 (2005).

3. J. E. Baldwin *et al.*, A substrate analogue study on clavaminic acid synthase: Possible clues to the biosynthetic origin of proclavaminic acid. *J. Chem. Soc. Chem. Commun.* **1993**, 500–502 (1993).
4. T. J. Kappock, J. P. Caradonna, Pterin-dependent amino acid hydroxylases. *Chem. Rev.* **96**, 2659–2756 (1996).

5. D. Lando *et al.*, FIH-1 is an asparaginyl hydroxylase enzyme that regulates the transcriptional activity of hypoxia-inducible factor. *Genes Dev.* **16**, 1466–1471 (2002).
6. T. Gerken *et al.*, The obesity-associated FTO gene encodes a 2-oxoglutarate-dependent nucleic acid demethylase. *Science* **318**, 1469–1472 (2007).
7. F. H. Vaillancourt *et al.*, Characterization of extradiol dioxygenases from a polychlorinated biphenyl-degrading strain that possess higher specificities for chlorinated metabolites. *J. Bacteriol.* **185**, 1253–1260 (2003).
8. B. G. Keenan, T. K. Wood, Orthric Rieske dioxygenases for degrading mixtures of 2,4-dinitrotoluene/naphthalene and 2-amino-4,6-dinitrotoluene/4-amino-2,6-dinitrotoluene. *Appl. Microbiol. Biotechnol.* **73**, 827–838 (2006).
9. Y. Mishina, C. H. Lee, C. He, Interaction of human and bacterial AlkB proteins with DNA as probed through chemical cross-linking studies. *Nucleic Acids Res.* **32**, 1548–1554 (2004).
10. S. Kal, L. Que, Dioxygen activation by nonheme iron enzymes with the 2-His-1-carboxylate facial triad that generate high-valent oxoiron oxidants. *J. Biol. Inorg. Chem.* **22**, 339–365 (2017).
11. E. I. Solomon, S. Goudarzi, K. D. Sutherlin, O<sub>2</sub> activation by non-heme iron enzymes. *Biochemistry* **55**, 6363–6374 (2016).
12. E. G. Pavel *et al.*, Circular dichroism and magnetic circular dichroism spectroscopic studies of the non-heme ferrous active site in clavamate synthase and its interaction with  $\alpha$ -ketoglutarate cosubstrate. *J. Am. Chem. Soc.* **120**, 743–753 (1998).
13. K. Valegård *et al.*, Structure of a cephalosporin synthase. *Nature* **394**, 805–809 (1998).
14. J. Zhou, M. Gunsior, B. O. Bachmann, C. A. Townsend, E. I. Solomon, Substrate binding to the  $\alpha$ -ketoglutarate-dependent non-heme iron enzyme clavamate synthase 2: Coupling mechanism of oxidative decarboxylation and hydroxylation. *J. Am. Chem. Soc.* **120**, 13539–13540 (1998).
15. J. N. Kemsley, N. Mitić, K. L. Zaleski, J. P. Caradonna, E. I. Solomon, Circular dichroism and magnetic circular dichroism spectroscopy of the catalytically competent ferrous active site of phenylalanine hydroxylase and its interaction with pterin cofactor. *J. Am. Chem. Soc.* **121**, 1528–1536 (1999).
16. M. S. Chow *et al.*, Spectroscopy and kinetics of wild-type and mutant tyrosine hydroxylase: Mechanistic insight into O<sub>2</sub> activation. *J. Am. Chem. Soc.* **131**, 7685–7698 (2009).
17. M. D. Krzyaniak, B. E. Eser, H. R. Ellis, P. F. Fitzpatrick, J. McCracken, Pulsed EPR study of amino acid and tetrahydropterin binding in a tyrosine hydroxylase nitric oxide complex: Evidence for substrate rearrangements in the formation of the oxygen-reactive complex. *Biochemistry* **52**, 8430–8441 (2013).
18. O. A. Andersen, T. Flatmark, E. Hough, High resolution crystal structures of the catalytic domain of human phenylalanine hydroxylase in its catalytically active Fe(II) form and binary complex with tetrahydrobiopterin. *J. Mol. Biol.* **314**, 279–291 (2001).
19. O. A. Andersen, A. J. Stokka, T. Flatmark, E. Hough, 2.0 Å resolution crystal structures of the ternary complexes of human phenylalanine hydroxylase catalytic domain with tetrahydrobiopterin and 3-(2-thienyl)-L-alanine or L-norleucine: Substrate specificity and molecular motions related to substrate binding. *J. Mol. Biol.* **333**, 747–757 (2003).
20. X. Zhang, J.-M. Beaulieu, T. D. Sotnikova, R. R. Gainetdinov, M. G. Caron, Tryptophan hydroxylase-2 controls brain serotonin synthesis. *Science* **305**, 217 (2004).
21. M. S. Windahl, J. Boesen, P. E. Karlens, H. E. M. Christensen, Expression, purification and enzymatic characterization of the catalytic domains of human tryptophan hydroxylase isoforms. *Protein J.* **28**, 400–406 (2009).
22. K. M. Roberts, J. A. Pavon, P. F. Fitzpatrick, Kinetic mechanism of phenylalanine hydroxylase: Intrinsic binding and rate constants from single-turnover experiments. *Biochemistry* **52**, 1062–1073 (2013).
23. J. Moore, J. M. Wood, K. U. Schallreuter, H<sub>2</sub>O<sub>2</sub>-mediated oxidation of tetrahydrobiopterin: Fourier transform Raman investigations provide mechanistic implications for the enzymatic utilization and recycling of this essential cofactor. *J. Raman Spectrosc.* **33**, 610–617 (2002).
24. G. Eberlein, T. C. Bruice, R. A. Lazarus, R. Henrie, S. J. Benkovic, The interconversion of the 5,6,7,8-tetrahydro-, 6,7,8-dihydro-, and radical forms of 6,6,7,7-tetramethylidihydropterin. A model for the biopterin center of aromatic amino acid mixed function oxidases. *J. Am. Chem. Soc.* **106**, 7916–7924 (1984).
25. S. O. Pember, S. J. Benkovic, J. J. Villafranca, M. Pasenkiewicz-Gierula, W. E. Antholine, Adduct formation between the cupric site of phenylalanine hydroxylase from *Chromobacterium violaceum* and 6,7-dimethyltetrahydropterin. *Biochemistry* **26**, 4477–4483 (1987).
26. K. Teigen, N. Å. Frøystein, A. Martinez, The structural basis of the recognition of phenylalanine and pterin cofactors by phenylalanine hydroxylase: Implications for the catalytic mechanism. *J. Mol. Biol.* **294**, 807–823 (1999).
27. O. A. Andersen, T. Flatmark, E. Hough, Crystal structure of the ternary complex of the catalytic domain of human phenylalanine hydroxylase with tetrahydrobiopterin and 3-(2-thienyl)-L-alanine, and its implications for the mechanism of catalysis and substrate activation. *J. Mol. Biol.* **320**, 1095–1108 (2002).
28. G. R. Moran, A. Derecskei-Kovacs, P. J. Hillas, P. F. Fitzpatrick, On the catalytic mechanism of tryptophan hydroxylase. *J. Am. Chem. Soc.* **122**, 4535–4541 (2000).
29. J. A. Pavon, B. Eser, M. T. Huynh, P. F. Fitzpatrick, Single turnover kinetics of tryptophan hydroxylase: Evidence for a new intermediate in the reaction of the aromatic amino acid hydroxylases. *Biochemistry* **49**, 7563–7571 (2010).
30. K. B. Patel, M. R. L. Stratford, P. Wardman, S. A. Everett, Oxidation of tetrahydrobiopterin by biological radicals and scavenging of the trihydrobiopterin radical by ascorbate. *Free Radic. Biol. Med.* **32**, 203–211 (2002).
31. M. Farahani *et al.*, Reactions of CO<sub>2</sub> – radicals with pterin and pterin-6-carboxylate ions. *J. Chem. Soc., Perkin Trans. 2* **1991**, 1687–1693 (1991).
32. S. D. Wong *et al.*, Elucidation of the Fe(IV)=O intermediate in the catalytic cycle of the halogenase SyrB2. *Nature* **499**, 320–323 (2013).
33. K. D. Sutherlin *et al.*, Nuclear resonance vibrational spectroscopy definition of O<sub>2</sub> intermediates in an extradiol dioxygenase: Correlation to crystallography and reactivity. *J. Am. Chem. Soc.* **140**, 16495–16513 (2018).
34. K. D. Sutherlin *et al.*, NRVs studies of the peroxide shunt intermediate in a Rieske dioxygenase and its relation to the native Fe<sup>II</sup> O<sub>2</sub> reaction. *J. Am. Chem. Soc.* **140**, 5544–5559 (2018).
35. A. R. Diebold *et al.*, Activation of  $\alpha$ -keto acid-dependent dioxygenases: Application of an FeNO<sub>7</sub>/FeO<sub>28</sub> methodology for characterizing the initial steps of O<sub>2</sub> activation. *J. Am. Chem. Soc.* **133**, 18148–18160 (2011).
36. P. F. Fitzpatrick, Kinetic isotope effects on hydroxylation of ring-deuterated phenylalanines by tyrosine hydroxylase provide evidence against partitioning of an arene oxide intermediate. *J. Am. Chem. Soc.* **116**, 1133–1134 (1994).
37. P. F. Fitzpatrick, Studies of the rate-limiting step in the tyrosine hydroxylase reaction: Alternate substrates, solvent isotope effects, and transition-state analogues. *Biochemistry* **30**, 6386–6391 (1991).
38. T. A. Dix, S. J. Benkovic, Mechanism of “uncoupled” tetrahydropterin oxidation by phenylalanine hydroxylase. *Biochemistry* **24**, 5839–5846 (1985).
39. S. Ye *et al.*, Electronic structure analysis of the oxygen-activation mechanism by Fe(II)- and  $\alpha$ -ketoglutarate ( $\alpha$ KG)-dependent dioxygenases. *Chemistry* **18**, 6555–6567 (2012).
40. A. J. Mitchell *et al.*, Visualizing the reaction cycle in an iron(II)- and 2-(Oxo)-glutarate-dependent hydroxylase. *J. Am. Chem. Soc.* **139**, 13830–13836 (2017).